Spatial characteristics of a zero-pressure-gradient turbulent boundary layer in the presence of free-stream turbulence

Eda Dogan,[1,2] R. Jason Hearst,[3,2,*] E. Ronald Hanson,[4,2] and Bharathram Ganapathisubramani[2]

[1] *Linné FLOW Centre, KTH Mechanics, Stockholm, SE-100 44, Sweden*
[2] *Engineering and the Environment, University of Southampton, Southampton, SO17 1BJ, United Kingdom*
[3] *Department of Energy and Process Engineering, Norwegian University of Science and Technology, Trondheim, NO-7491, Norway*
[4] *Department of Mechanical Engineering, York University, Toronto, Ontario M3J 1P3, Canada*

(Dated: August 5, 2019)

Particle image velocimetry (PIV) measurements are performed to examine the structural organisation inside a turbulent boundary layer under the influence of free-stream turbulence (FST). In particular, streamwise-wall-normal plane PIV measurements are presented for two cases at two different turbulent intensity levels (about 12% and 8%). The high-intensity free-stream turbulence is generated using an active grid in a wind tunnel. The statistical information of the flow regarding the wall-normal velocity and Reynolds shear stress are presented. The effect of increasing the turbulence level in the free stream for these flows has been found to have similarities with increasing Reynolds number for high Reynolds number canonical flows. Quadrant analysis is performed to determine the contributions of different Reynolds-stress-producing events. In this regard, the distribution of momentum transport events shows some similarity with channel flows, which can be justified by comparison of similar intermittency characteristics of both flows. In addition, the coherent structures found inside the boundary layer have inclined features that are consistent with the previous studies for canonical flows. The fact that the external disturbance, such as FST in this study, does not alter the organisation of the structures inside the boundary layer supports the growing evidence for a universal structure for wall-bounded flows.

* jason.hearst@ntnu.no

I. INTRODUCTION

Free-stream turbulence (FST) is a major external disturbance for turbulent boundary layers encountered in many natural and industrial flows. The effects of FST on turbulent boundary layers include enhanced heat transfer and increased skin friction [1, 2], which can be both beneficial and detrimental for the performance of an engineering device. FST length scales penetrate into the boundary layer, which changes in the nature of momentum and energy transport within, through interactions between those imparted and those already existing in the boundary layer. The effect of FST on boundary layer transition mechanisms was studied by Hunt *et al.* [3]. More recently, the analysis of the effects of FST penetration inside turbulent boundary layers are considered by Sharp *et al.* [4] and Dogan *et al.* [5, 6] in terms of scale interactions. Sharp *et al.* [4] found similarities in energy distributions inside the boundary layer to the ones occurring in canonical turbulent boundary layers at similar Re_τ, which is the friction-velocity based Reynolds number defined as $U_\tau\delta/\nu$ where U_τ is the friction velocity, δ is the boundary layer thickness and ν is the kinematic viscosity. Dogan *et al.* [5, 6] expanded this observation by providing near-wall turbulence statistics through single-wire measurements. This methodology was particularly useful towards demonstrating that the large scales in the outer region have a modulating effect on the small scales in the near-wall region and this effect becomes more prominent with increasing FST level, which was found similar to the effect of increasing Re_τ in high Reynolds number flows. The analogy between turbulent boundary layer having high levels of FST at moderate Re, and high-Re at low FST levels is based on large energetic motions in the outer region in boundary layers, known as superstructures, become more energetic and their footprint in the near-wall region becomes more important with increasing Re_τ. These superstructures carry a significant portion of the turbulent kinetic energy, contributing to a significant amount of the Reynolds stresses in these flows [7–9].

The generation of Reynolds shear stress is governed by the momentum transport events and is believed to be the main source for production of turbulence and increased surface drag. The turbulence producing events in a canonical boundary layer include: "ejections" as low-speed fluid close to the wall is pushed away from the wall and "sweeps" as high-speed fluid is moved towards the wall. For boundary layers under the influence of FST, very limited information is available on multi-component velocity measurements. Two velocity component information is available either by cross-wire measurements [2, 4, 10, 11] or LDV [12]. The focus of the turbulence statistics in these studies was mainly on the mean Reynolds shear stress, the mean and rms of the velocity fluctuations. However, little information on the spatial structure of the turbulent flow exists for this scenario. The objective of the present research is to address this through detailed spatial correlation information in a turbulent boundary layer subjected to FST.

In this experimental study, planar particle image velocimetry (PIV) measurements are performed to examine the spatial structure as well as the momentum transport events in boundary layers under the influence of FST. In particular, streamwise-wall-normal plane PIV measurements will be presented for two cases at two different turbulence intensity levels. The distribution of the velocity fluctuations in the context of the momentum flux events will be discussed in detail. Finally, length scales and coherence in the flow obtained using the two-point correlations will also be discussed.

II. EXPERIMENTAL PROCEDURE

The experiments were performed in an open-circuit suction type wind tunnel at the University of Southampton. The tunnel has a 0.9 × 0.6 × 4.5 m cross-section and a turbulent boundary layer was established on a suspended floor. Free-stream turbulence was generated with an active grid. This grid contains 11 vertical and 7 horizontal rod arrays that have wings attached on them and can be independently controlled by stepper motors and is based on the original design by Makita [13]. Detailed information on the facility and active grid design are found in Dogan *et al.* [5].

Planar PIV measurements were performed to enable the analysis of the instantaneous spatial features of the turbulent boundary layer in the presence of FST. Three LaVision ImagerProLX CCD 16 mega-pixel cameras fitted with Nikon Nikkor lenses with a focal length of 200 mm at an f-stop (aperture) of 8 were used to image the measurement plane. The cameras were oriented in a T-shaped formation to acquire both the boundary layer and the free-stream with field of view of each camera overlapping by 1 cm. The leading edge of the measurement plane is approximately 3.2 m downstream of the mid plane of the active grid. The field of view was about 32 cm × 27 cm. The laser sheet was generated by a Litron Lasers Nano L200 15PIV Nd:YAG laser (532 nm wavelength, 200 mJ/pulse, 15 Hz repetition rate) and illuminated a streamwise-wall-normal plane perpendicular to the test plate. The experimental arrangement described is shown in Figure 1. The time delay between laser pulses was chosen as 70 μs to optimize the accuracy of the measurements. The flow was seeded with particles of a glycol and de-mineralised water solution. In total, 2000 images were acquired and then were processed with LaVision DaVis 8.2.2. Owing to the large measurement region of interest, and the known adverse effect of peak locking [14], the potential effects were mitigated using the algorithm

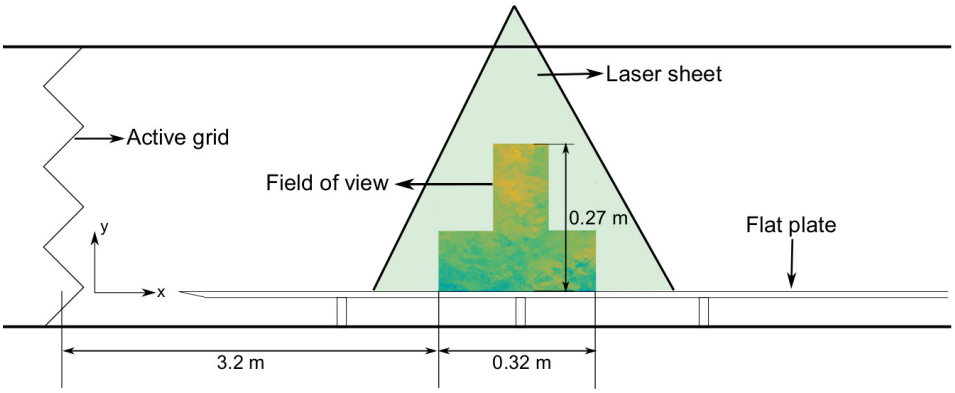

Figure 1. Schematic of the test section with illuminated field of view (not to scale)

developed by Hearst and Ganapathisubramani [15]. The application of this method is as follows. The images were pre-processed by first applying a sliding background subtraction filter to reduce noise, and then applying a 3 × 3 Gaussian kernel filter to slightly blur the particles over more pixels; the latter helps to reduce the influence of pixel-locking. The vector fields were then computed using 50% overlap and five passes reducing from 96 pixels × 96 pixels windows to 16 pixels × 16 pixels windows. Window deformation was used on final passes to mitigate pixel-locking. Finally, the vectors were post-processed by applying histogram equalisation on a vector-by-vector basis as described by Hearst and Ganapathisubramani [15] to further diminish the influence of pixel-locking.

III. FLOW CONDITIONS AND BOUNDARY LAYER STATISTICS

In this study, two representative FST cases, B and D, from Dogan *et al.* [5], are considered. Case D is an example of high FST whereas case B is an example of low FST. The naming convention is retained for consistency. It should be noted that the FST levels in both these cases (about 12% and 8%, respectively, for high and low) are still significantly higher than most previous studies that have examined the effects of FST. The active grid protocol for each case is reproduced from Larssen and Devenport [16] from their test case 14. These two cases only differ by their blockage ratio depending on which wings were used, either solid wings or cut-out wings with holes. This will generate a free-stream turbulence with similar length scales and isotropy but with different turbulence intensity levels [17]. Single-point hot-wire measurements were performed in Dogan *et al.* [5] allowing very near-wall statistics and the Preston tube method was implemented to obtain the skin-friction values. Oil Film Interferometry was later applied to validate the Preston-tube estimates of skin-friction values [18].

A comparison of the mean and variance of streamwise velocity from PIV and hot-wire for the test cases are provided in Figure 2. Inner scaling is used to normalise the velocities and wall-normal position, i.e. the length and velocity quantities are normalised by ν/U_τ and U_τ, respectively. The convention throughout the paper is that the capital letter for a velocity in a certain direction is given for its mean value whereas the lower case refers to its fluctuating component. Although the near-wall statistics are only resolved with high resolution for the hot-wire measurements, the close resemblance between the two profiles throughout the rest of the boundary layer provides confidence in the current measurements. The mean profiles in Figure 2(a) show a distinctly suppressed wake region and an extended logarithmic region with the log-law coefficients $\kappa = 0.384$ and $B = 4.4$. The most prominent feature of the variance profiles of the streamwise velocity, Figure 2(b), is the increase in the near-wall peak amplitude with increasing turbulence intensity. This is consistent with the effect of increasing Reynolds number in high Reynolds number flows. A detailed discussion of this observation is given by Dogan *et al.* [5].

Flow parameters of the test cases are presented in Table I. The subscript "0" is used to denote parameters calculated from the free-stream. The boundary layer thickness, δ, from PIV measurements is defined as the height at which the mean turbulence intensity profile is within 1% of the turbulence intensity in the free-stream. This method was preferable to the traditional definition of δ_{99}, such as that of Perry and Li [19], where an iterative approach is used to estimate δ_{99}. The latter was found to fail for the PIV data owing to a combination of random uncertainty in the free-stream measurement and insufficient near wall resolution, which resulted in poor convergence of the integral scheme. The Taylor micro-scale, λ_0, Reynolds number, $Re_{\lambda_0} = \sqrt{\overline{u_0^2}}\lambda_0/\nu$, and friction velocity, U_τ, are taken from Dogan *et al.* [5], where these parameters were determined from measurements made using a single hot-wire probe and Preston tube, respectively. In the present study, the PIV measurements enable us to focus on the wall-normal velocity

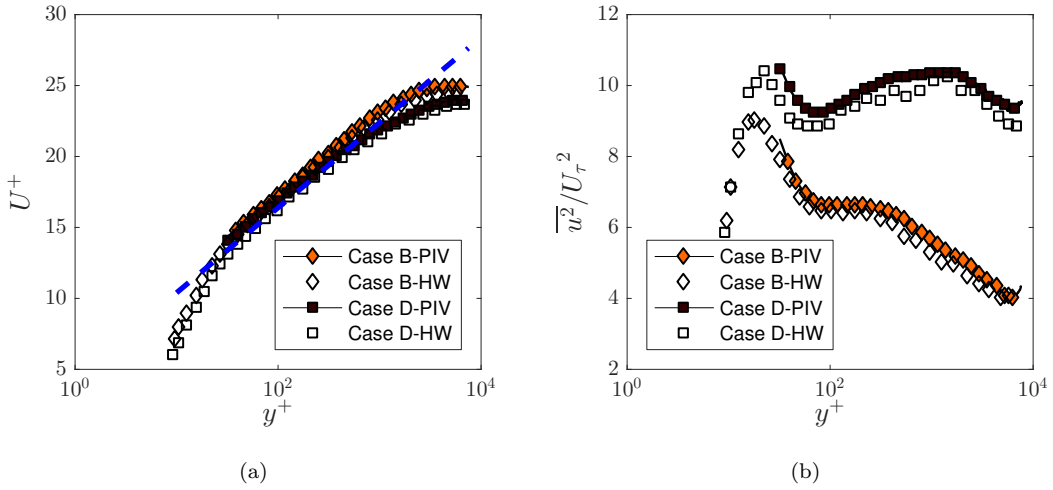

(a) (b)

Figure 2. (a) Mean and (b) variance profiles of the streamwise velocity component in inner scaling from PIV and hot-wire in comparison. Dashed line in (a) is the log-law line with coefficients $\kappa = 0.384$ and $B = 4.4$. Markers on the PIV data curve are undersampled for clarity. Symbols are explained in the legend.

FST cases	U_0 (m/s)	$\sqrt{\overline{u_0^2}}/U_0$ (%)	Re_{λ_0}	δ (mm)	θ (mm)	U_τ (m/s)	Re_τ	Re_θ
B (diamond)	10.2	8.1	505	176	6.8	0.41	4640	4330
D (square)	10.1	12.2	645	183	8.0	0.42	4930	5130

Table I. Free-stream and turbulent boundary layer parameters for the study cases. U_0: mean streamwise velocity of the free-stream, $\sqrt{\overline{u_0^2}}/U_0$ (%): free-stream turbulence intensity, Re_{λ_0}: Reynolds number based on free-stream Taylor microscale, δ: boundary-layer thickness (defined in the text), U_τ: friction velocity, Re_τ: Reynolds number based on friction velocity, Re_θ: Reynolds number based on momentum thickness

component and Reynolds shear stress for turbulence statistics to previous accessible from single-wire measurements.

A. Wall-normal velocity

The inner and outer scaled mean wall-normal velocity profiles are shown in Figure 3. The ability for inner-scaling, Figure 3(a), to result in near-wall similarity is significant since it suggests that the effect of the turbulence level in the free-stream results in a comparable increase in the skin friction, U_τ. However, past $y^+ > 100$, this collapse is no longer evident, which aligns with the mid log-region where FST occurs due to direct penetration. Considering Figure 3, the case having higher turbulence level in the free-stream results in an increase in the mean wall-normal velocity component.

Recently, a outer scaling method was proposed for the mean wall normal velocity component by Wei and Klewicki [20]. This scaling of the mean wall normal velocity by V_0 is reproduced in Figure 3(b). Some improvement in the similarity is noticeable in the wake and outer region for $y/\delta > 0.1$, however, a complete similarity is lacking and the reasons for this are unknown. Nonetheless, the improved similarity found in the outer region suggests that this scaling may capture the local effects caused by the presence of free stream turbulence, however, the combined near-wall and log-region variation gives evidence of a more complex phenomena in these cases. It is possible that the free-stream turbulence and the degree of randomness inflicted by its presence reduces the fidelity of this scaling.

The variance profiles of the wall-normal velocity fluctuations are given in comparison with the channel flow data from Lozano-Durán and Jiménez [21] at a comparable Re_τ in Figure 4. This comparison to channel flow is motivated from the previous observations by Dogan *et al.* [5] for the streamwise velocity component from their hot-wire measurements which showed similarities between the two flows, i.e. channel flows and turbulent boundary layers under FST effect. This similarity is especially found in the wake region where the intermittency is lost for these two flows, with the presence of a turbulent core in the centreline of the channel and the FST, respectively. For wall-normal velocity fluctuations, the lower turbulence case seems to follow the channel flow data better than the higher turbulence case.

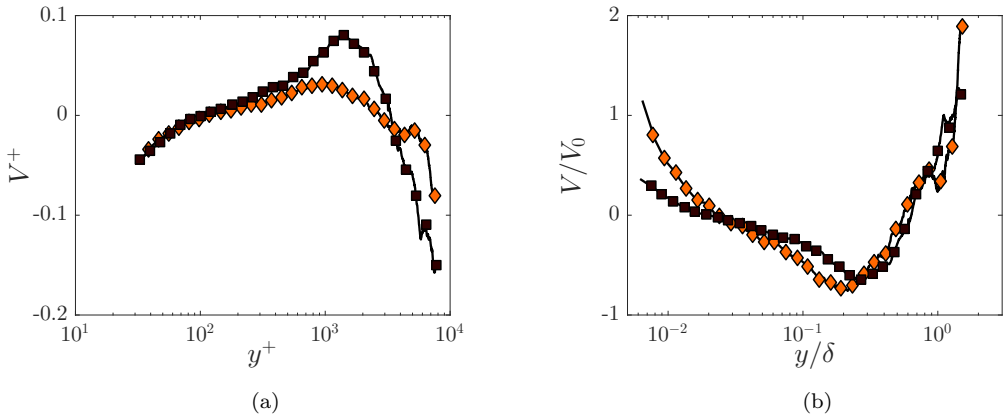

Figure 3. Mean wall-normal velocity profile in (a) inner-scaling (b) outer scaling proposed by Wei and Klewicki [20]. Markers on the PIV data curve are undersampled for clarity. Case B: filled diamond, case D: filled square.

The near-wall similarity up to mid-log region is observed. The similarity of the profiles sustains until the point FST cases peel up with the intense wall-normal fluctuations due to the presence of turbulence in the free stream. It has been shown in the literature for high Reynolds number flows that the wall-normal fluctuations exhibit a nearly constant extended plateau [22–24]. It is worth mentioning that the analogy of the turbulent boundary layer flows under the effect of FST with high Re flows, which is detailed in Dogan *et al.* [5, 6], is further supported here with the plateau region observed in the wall-normal variance profiles.

The distinction between the wall-normal variance profiles of the two FST cases is more obvious for $y^+ > 1000$ and approaching the free stream as expected due to their different free-stream turbulence levels. This suggests that the free-stream turbulence appears to set the skin-friction velocity and the flow responds proportionally to the increase in skin-friction. This may be understood by considering that the integrated momentum flux over the thickness of the boundary layer is related to the drag (i.e. skin friction) of the surface. Therefore, the velocity fluctuations should, in turn, scale with skin-friction velocity. Regardless, the degree of similarity between the three profiles in the inner region is remarkable. The fidelity of this scaling for the momentum flux (i.e. Reynolds shear stress) is also examined later in the paper. The right axis of the figure (blue outlined) is given as normalised with the variance of the streamwise velocity fluctuations of the free-stream. This would also give information about the isotropy of the flow in the free-stream. The isotropy ratio can be defined as $I = \frac{\sqrt{\overline{u_0^2}}}{\sqrt{\overline{v_0^2}}}$. The isotropy (or anisotropy thereof) is found to be around 1.4 for case B and around 1.3 for case D. These values are slightly higher than the previous active grid studies that similarly followed Makita's original active grid design [16, 25]. However, the anisotropy is mostly associated with the largest scales of the flow and since in this study the u fluctuations are forced to be large-scale (such that the spectral peak was at 10δ), the lack of isotropy is expected.

B. Reynolds shear stress profiles

Figure 5(a) shows the shear stress correlation coefficient, also known as velocity correlation coefficient. For higher turbulence case, this coefficient is lower as expected since the penetration is greater for this case. The effect of the penetration of uncorrelated, large-scale FST is to reduce the correlations. This effect is also shown in Hancock and Bradshaw [10] and Thole and Bogard [12] for boundary layers under the effect of FST. They also suggested that these uncorrelated large-scales from the free-stream have only small contribution to Reynolds shear stress in the inner region. For canonical flows, this is similarly observed with increasing Reynolds number [22, 26]. Priyadarshana and Klewicki [26] showed that at high Reynolds number, the spectral overlap between the u and v signals is reduced, thereby reducing the correlation between the two; however, they did not observe an apparent effect in the Reynolds shear stress. To illustrate this for the present FST cases, Figure 5(b) shows profiles of Reynolds shear stress. The wall-normal location is plotted in inner-coordinates while the shear stress is normalised by friction velocity. The figure shows, as suggested previously, that although for higher turbulence case the penetration is higher, it does not result in higher mean values for the inner-scaled Reynolds shear stress. Also in this figure, the channel flow

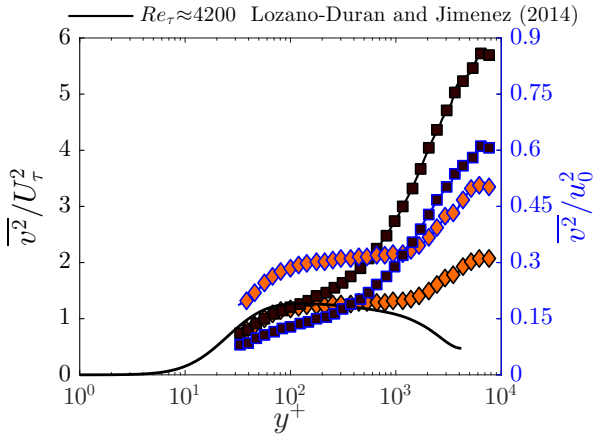

Figure 4. Variance profiles of the wall-normal velocity fluctuations. The ordinates show the profiles in (left) inner-normalised and (right) normalised by the variance of the free-stream streamwise velocity fluctuations (blue outlined). Markers on the PIV data curve are interpolated data points for clear representation. Case B: filled diamond, case D: filled square.

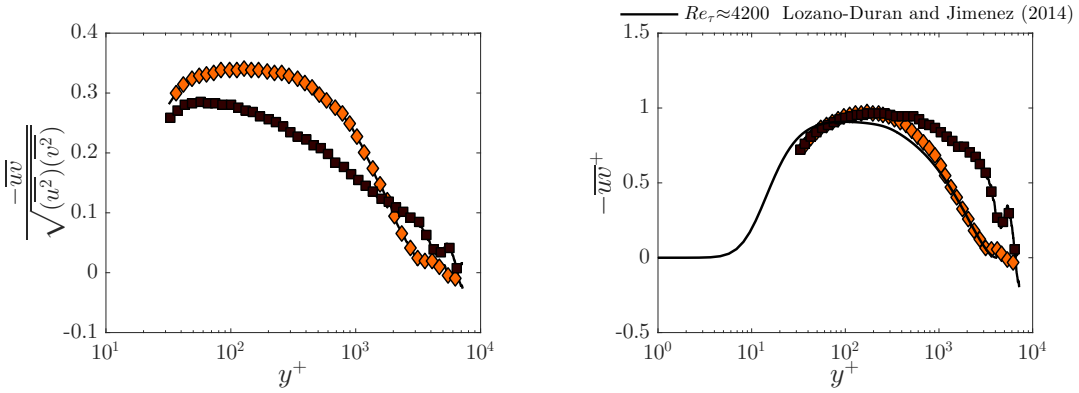

Figure 5. (a) Shear stress correlation coefficient and (b) inner-normalised Reynolds shear stress profiles. Markers on the PIV data curve are interpolated data points for clear representation. Case B: filled diamond, case D: filled square.

data from Lozano-Durán and Jiménez [21] is plotted as comparison. Low-range turbulence case B seems to follow the channel data better than high turbulence case D. Once again, despite the large amount of disturbance in the free-stream, the momentum flux in the near-wall region appears to scale with local skin-friction velocity regardless of the turbulence intensity in the free-stream. This is consistent with the observations for the vertical component. However, this behaviour is markedly different from the behaviour of the streamwise velocity component where the inner-scaling with friction velocity did not collapse the profiles in this region. It is also worth noting that the shear stress profiles exhibit an extended plateau region with increasing turbulence level. This is also similar to observations in high Reynolds number canonical flows where the extent of the plateau increases with increasing Re_τ.

Figure 6 shows two snapshots of the instantaneous Reynolds shear stress for a representative FST case. Considerable amount of Reynolds shear stress production can be detected instantaneously from these snapshots, i.e. uv product values as high as $10U_\tau^2$. With the addition of more turbulence in the free-stream (case D), this has been observed to increase even more (figure not shown here). These instantaneous momentum transport events can be characterised by examining its distribution through the boundary layer and comparing this to other canonical flows.

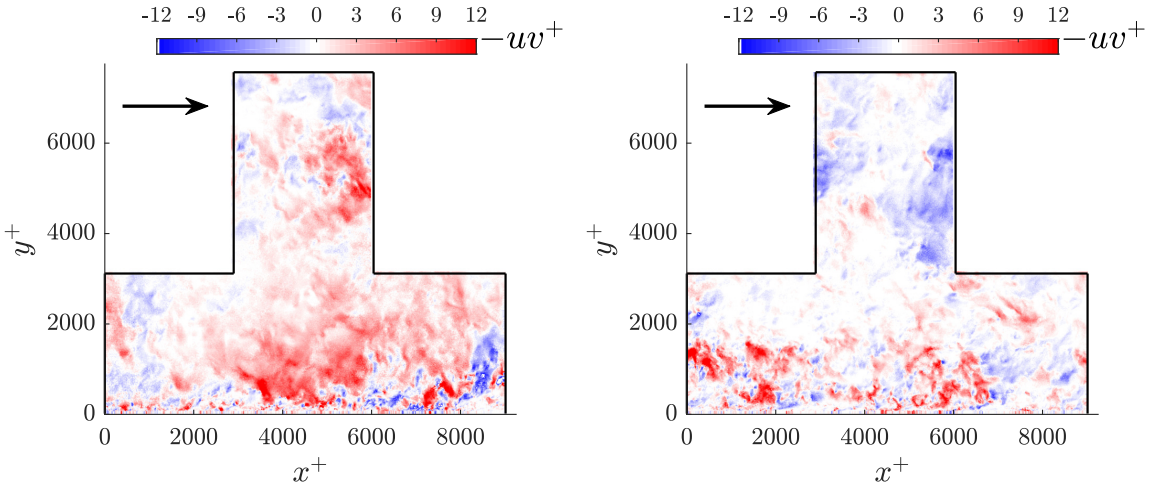

Figure 6. Contour plot of two snapshots of instantaneous inner-normalised Reynolds shear stress ($-uv^+$) for case B. The enclosed region shows the data from the field of view. Flow is from left to right as indicated by the arrow on top left.

C. Distribution of uv events

After examining the mean profiles of the Reynolds shear stress, it is important to see how uv events are distributed across the boundary layer. Figure 7 shows the contour maps of the normalised probability density functions (pdfs) of instantaneous shear stress for the two FST cases. Across the whole boundary layer, both pdfs are skewed towards negative values which is consistent with the sign of the mean Reynolds shear stress (Figure 5(b)). This demonstrates that the dominant contributions to total Reynolds stresses are from negative shear stress events of sweeps ($u > 0$, $v < 0$) and ejections ($u < 0$, $v > 0$) and they outweigh the contributions from positive shear stress events of inward ($u < 0$, $v < 0$) and outward ($u > 0$, $v > 0$) interactions.

When profiles are extracted at various wall-normal locations, the distributions for both FST cases can be compared as done in Figure 8. At $y^+ \approx 100$, where the mean Reynolds shear stress showed similarity in Figure 5(b), the pdfs seem to differ for the most intense uv events, i.e. at the tails of the distribution. This shows the effect of increasing turbulence intensity on the intense ejection and sweep events. This again is analogous to an increase in Reynolds number for a canonical wall-bounded flow [27]. For an outer region location, at $y/\delta \approx 0.2$, the higher turbulence case shows a clear distinction in the distribution as also deduced from the mean Reynolds shear stress profile where the two FST cases differ.

IV. QUADRANT ANALYSIS

The above analysis, as expected, showed that the probability distribution of uv is skewed towards negative events. To further quantify the contributions, conditional averaging of this product is needed and here it is based on the analysis introduced by Wallace *et al.* [28] and Lu and Willmarth [29]. They suggested that there is useful information contained in the signs of the individual velocity fluctuations. They also exploited this by classifying the products of these fluctuations into four categories which they later called quadrants of the Reynolds shear stress plane: Q1 ($+u$, $+v$), Q2 ($-u$,$+v$), Q3 ($-u$, $-v$), and Q4 ($+u$, $-v$). Events in the second quadrant, Q2, correspond to negative streamwise fluctuations (low-speed) being lifted away from the wall by positive wall-normal fluctuations, and they are referred to as *ejections*. Events in the fourth quadrant correspond to positive streamwise fluctuations (high-speed) being moved towards the wall by negative wall-normal fluctuations and these motions are called *sweeps*. Q1 and Q3 are called outward and inward interactions. This type of quadrant analysis does not specify the form of the eddies creating sweeps and ejections, but it permits the analysis of the contribution of these events to the total mean values of various quantities [30].

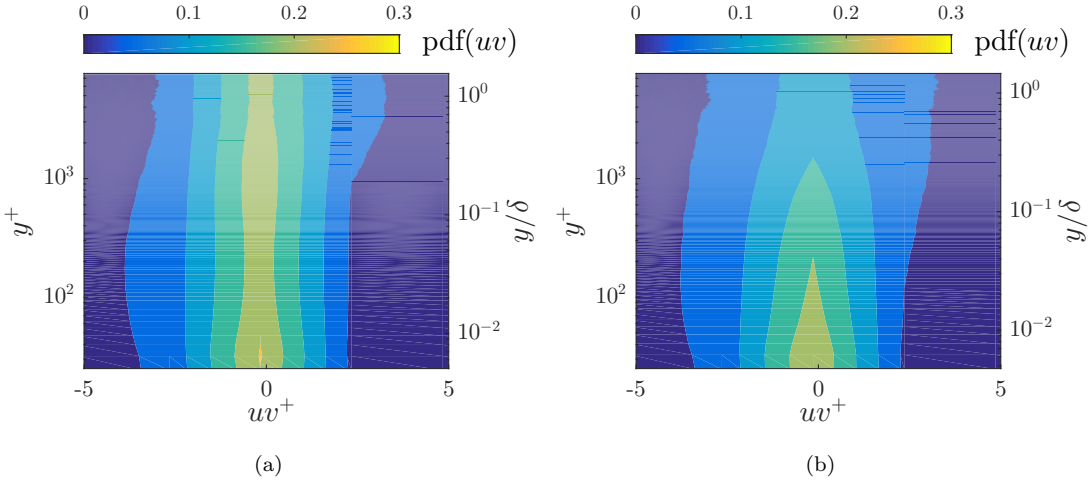

Figure 7. Contour maps of the normalised pdf of uv. The ordinates show the wall-normal location in inner (left) and outer (right) scaling. (a) case B (b) case D.

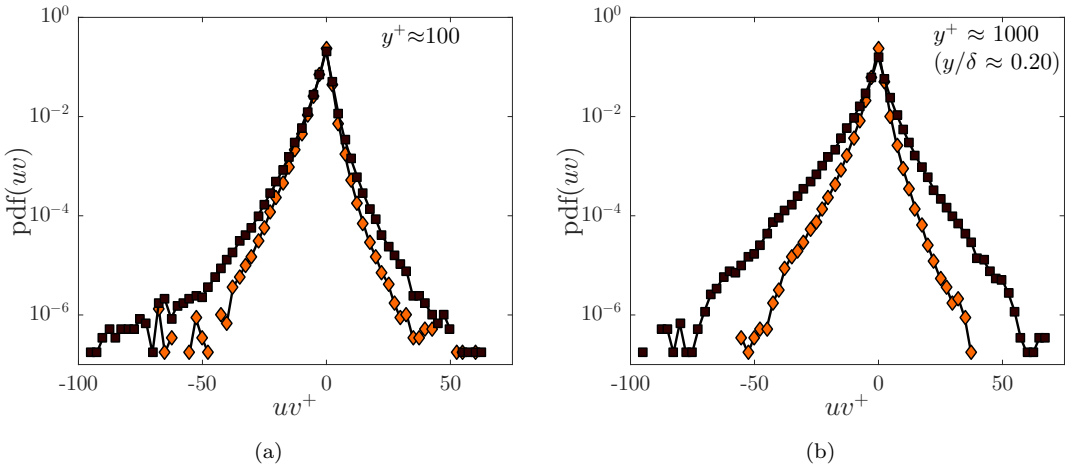

Figure 8. Comparison of the pdfs of the two FST cases at two wall-normal locations (a) y^+≈100 (b) y/δ≈0.2. Case B: filled diamond, case D: filled square.

The Reynolds shear stress can be written as follows:

$$\overline{uv} = \int\int_{-\infty}^{\infty} uvP(u,v)dudv \tag{1}$$

where $P(u,v)$ is the joint probability density function and $uvP(u,v)$ is the covariance integrand, i.e. a weighted joint pdf. The integral of the latter distribution over a differential area $dudv$ represents the contribution of that particular pair of u and v to the covariance $\overline{uv}$ both in sign and magnitude. When plotted on $u-v$ plane, this covariance integrand will be zero on each axis by its definition; therefore, the distribution of contributions to Reynolds shear stress will be distinctly split into four quadrants.

Figure 9 shows covariance integrands of u and v at various wall-normal locations for both FST cases. The larger contributions are clearly seen to be from Q2 and Q4 events for both cases. In these quadrants, for the high turbulence case D, the extent of the elliptical shape of the covariance integrand is greater. This shows the effect of increasing turbulence level in the free-stream on the intensity of these quadrant events. As the distance from the wall increases towards the free-stream, the elliptical shape of the weighted joint pdf becomes more circular and the fractional contributions from Q1 and Q3 events also increase. For a turbulent boundary layer with no-FST, the ejections (Q2 events) are known to be dominant above the buffer layer throughout the boundary layer [29, 31]. However, for a

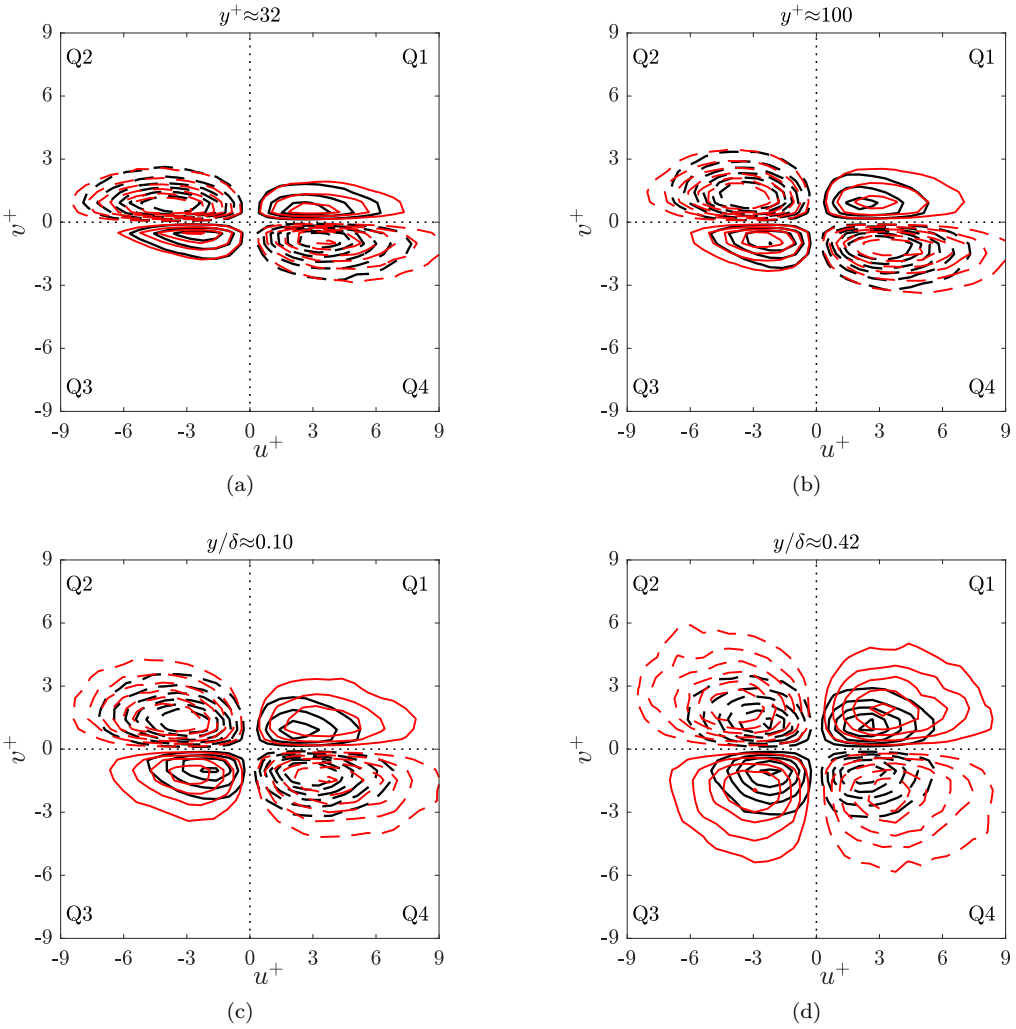

Figure 9. Covariance integrands of u and v fluctuations for case B (black colour) and case D (red colour) at various wall-normal locations: (a) $y^+\approx32$, (b) $y^+\approx100$, (c) $y/\delta\approx0.1$ and (d) $y/\delta\approx0.42$. Negative contours are shown with dashed lines. The outermost contour level is ±0.01 and the increment is 0.01 for positive contours and -0.01 for negative contours. Zero contours are not shown.

turbulent boundary layer under the effect of FST, the contribution from sweep events is comparable to the contribution from ejections and it even outweighs for high turbulence case D. This can be justified with the penetration of free-stream fluctuations into the boundary layer, i.e. increasing negative wall-normal velocity fluctuations (Figure 3). Comparing the two FST cases, the collapse of the contour maps inside the logarithmic region, Figure 9(a) and 9(b), is remarkable while in the outer region, high intensity FST case essentially shows higher fluctuations indicating the direct impact of the FST penetration.

To focus on the intense occurrences of the Reynolds shear stress, Willmarth and Lu [32] extended the quadrant analysis by introducing a hole filtering. The uv plane is divided into five regions as schematically shown in Figure 10(a). In the figure, the shaded region is called "hole" and is bounded by $|uv|$ = constant lines. Here, a hole size, h, is defined as a threshold to exclude uv events of small magnitude to determine the relative contributions of the more intense uv events. The fractional contributions from each quadrant, Q, can be calculated with the relation given below following Lu and Willmarth [29].

$$\frac{\widetilde{uv}_{|_{Q_i}}}{\overline{uv}} = \frac{1}{\overline{uv}}\left(\frac{1}{N}\sum_{n=1}^{N} uv_{|_i} S_i(h)\right) \qquad i = 1,4 \quad (2)$$

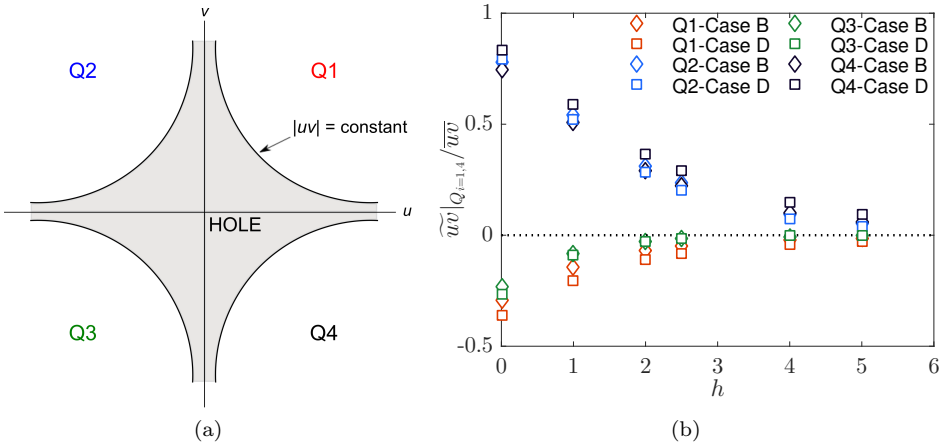

Figure 10. (a) Schematic illustrating quadrant splitting of the $u-v$ plane with shaded hole region (b) Fractional contributions to the Reynolds shear stress by each quadrant at $y^+\approx40$ for various hole sizes, h, for both FST cases. Symbols are explained in the legend.

and where N is the total number of samples and

$$S_i\left(h\right)=\begin{cases}1, & \text{if } |uv| \geq h\sqrt{\overline{u}}\sqrt{\overline{v}} \text{ and } (u,v) \text{ pair is in the } i^{th} \text{ quadrant of the } u-v \text{ plane,}\\ 0, & \text{otherwise}\end{cases} \tag{3}$$

Different hole sizes are tested as representatively illustrated for a wall-normal location of $y^+\approx40$ in Figure 10(b). Bogard and Tiederman [33] reported that the optimum threshold for the buffer region is $h\approx1$, based on direct comparisons between the detected events and instantaneous visualisations of the flow. Lozano-Durán *et al.* [34] were also able to show comparable results for bursts in the buffer region for their threshold value of 1.75. They also observed that their results are qualitatively similar within the range of $1 \leq h \leq 3$. For the present study, the value of h is set at 2, which is located midway in the aforementioned range.

Figure 11 presents quadrant contributions with a hole size of $h = 2$ for both cases of FST. It is obvious that the dominant contributors are Q2 and Q4 events for both cases. The outward and inward interactions, Q1 and Q3, respectively, contribute very little to the total Reynolds shear stress. These interaction events have been observed to be more active towards the edge of the boundary layer in the presence of FST as opposed to a canonical turbulent boundary layer. This feature is similarly found in channel flows as the increased contribution of the two dominant quadrants, Q2 and Q4, near the centreline of the channel is compensated by a parallel increase of the contributions from the quadrants Q1 and Q3 [31]. This similarity can be justified by common intermittency characteristics of the two flows, i.e. channel flow and the turbulent boundary layer under the FST effect. Sweeps are slightly more dominant for high turbulence case D than low turbulence case B up to $y/\delta\approx0.5$. This could be explained by stronger penetration of FST for case D. The contributions from sweeps and ejections for case D seem to be almost equal across the boundary layer. For case B, the ejections seem to be the main contributor to the Reynolds shear stress. This shows that the near-wall fluctuations are still dominant in their own right for this case.

The ratio of Q2 to Q4 events is given in Figure 12. Ejections seem to be dominant for almost the whole boundary layer for low turbulence level case B. On the other hand, for case D, sweeps are dominant up to $y/\delta\approx0.1$ from which ejections take over. It is also interesting to note that the ratio Q2/Q4 exhibits higher values for low turbulence case B than high turbulence case D. It is possible that, for case B, the near-wall ejections did not encounter as strong suppression from sweeps towards the wall as it is for case D. This also reveals the robustness of near-wall ejections despite high free-stream fluctuations for both cases. This ratio stays in the range 1.5-2 for channel flows and reaches 3 for a canonical boundary layer at $y\approx\delta$ [31]. For the present study, this ratio is more similar to that of channel flows, over the values observed for canonical turbulent boundary layer flows.

Quadrant analysis is useful to quantify the distributions of the events associated with the high- and low-speed fluid motions. However, it does not directly provide an indication of the spatial scales that contribute to these events. Velocity correlations can provide a great deal of insight of the spatial distribution of how these high- and low-speed fluid regions manifest in the flow. For this purpose, the focus of the next section is on the two-point spatial correlations.

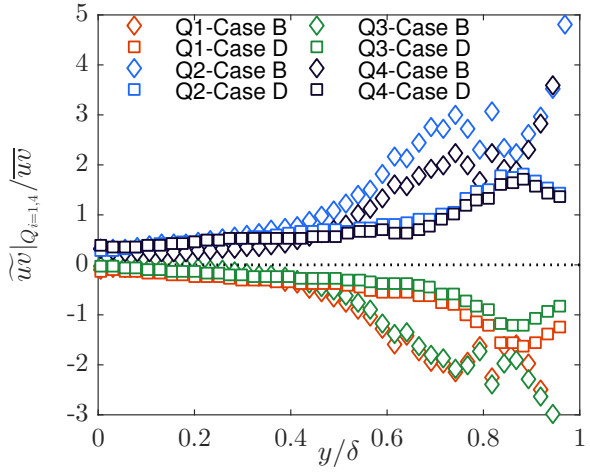

Figure 11. Distribution of quadrant contributions based on the hole size of $h = 2$ for both FST cases. Symbols are explained in the legend.

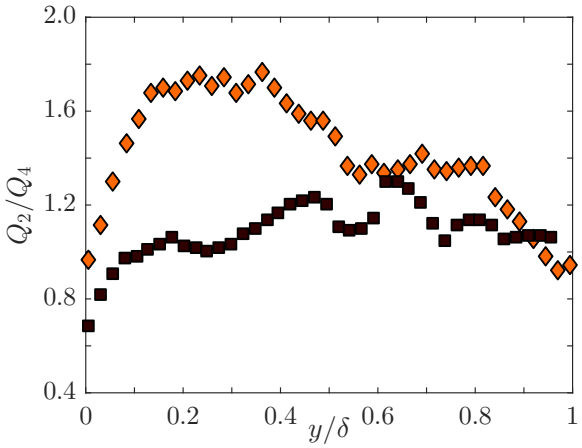

Figure 12. Distribution of the ratio Q2/Q4. Case B: filled diamond, case D: filled square.

V. VELOCITY CORRELATIONS

To provide an estimate of the dimensions of the scales that are involved in generating Reynolds shear stress and in creating the coherent motions of sweeps and ejections, two-point space-time correlations are useful. In a shear flow, when the variable measurement location is displaced throughout the flow relative to a fixed measurement location, the shape and extent of the iso-correlation contours reveal information about the shape and size of the flow structures underlying the correlation [35]. The streamwise-wall-normal plane spatial correlations can be computed using planar PIV data. The two-point correlation coefficient between any two quantities, R_{AB}, is defined as [36]:

$$R_{AB} = \frac{\overline{A\,(x,y)\,B\,(x+\Delta x, y+\Delta y)}}{\sigma_A \sigma_B} \tag{4}$$

where, σ_A and σ_B are the standard deviations of the quantities of interest A and B, respectively, and Δx and Δy are the streamwise and wall-normal spatial separations, respectively, between these two components. Multiple realisations are ensemble averaged to obtain the correlation coefficient and the overline notation denotes this averaging. Based on this definition, velocity correlations are computed at every wall-normal location in each relation to every other location in the boundary layer. Figure 13 shows the two-point auto-correlations for the streamwise velocity fluctuations, R_{uu}, computed at different wall-normal locations for both cases. Note the abscissa shows the streamwise distance in both upstream and downstream distance.

In the near-wall (Figure 13a), the contour lines are confined to a relatively small region. As the reference wall-

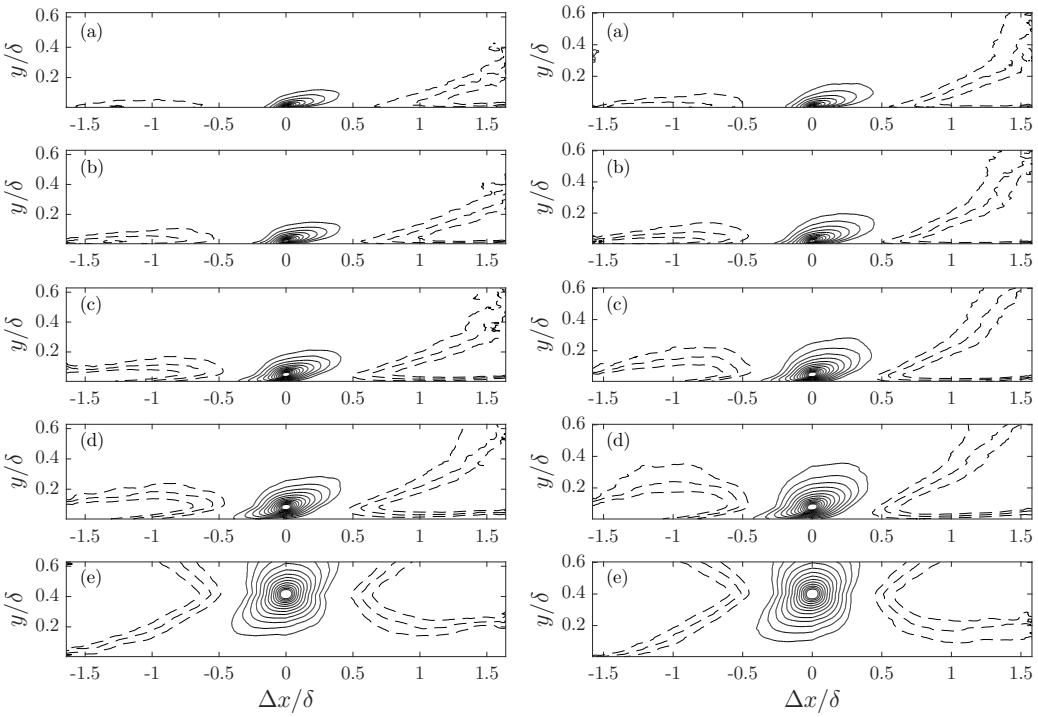

Figure 13. R_{uu} correlation computed at different wall-normal locations. (a) y^+≈40 (b) y^+≈100 (c) y^+≈240 (d) y^+≈400 (e) y/δ≈0.4. (Left) case B (right) case D. Negative contours are shown with dashed lines. The outermost contour level is ±0.1 and the increment is 0.05 for positive contours and -0.05 for negative contours. Zero contours are not shown.

normal location for the correlation calculations move away from the wall, i.e. in the log layer and above (Figure 13b-e), the contour lines are more elongated and cover an extended region as similarly observed in canonical flows ([36, 37] among many others). Correlation contours weaker than 0.1 are not shown on the figure; however, it has been noticed that the outer layer is physically connected to every other layer of the boundary layer down to the wall, albeit weakly correlated. This shows the coherence of the structures inside the boundary layer even in the presence of FST. The negative correlations appear to be stronger and more elongated at higher wall-normal locations in the boundary layer. The wall-normal extent of these negatively correlated structures is observed to significantly increase above the log-region (Figure 13e). The field of view of the present measurements is too short to capture the entire extent of these elongated structures. The positive correlations have inclined features which will be discussed in more detail in the following paragraphs.

To be able to compare the structure sizes for both FST cases, Figure 14 presents a specific contour level tracked for these cases for the wall-normal locations chosen above also for Figure 13. There is very little difference in the extent and shape of the structures between the two cases. Even the way these structures are inclined seem to be similar for both cases. This suggests that the change in the free-stream turbulence level does not affect the structural organisation of the flow in the streamwise-wall-normal plane. This finding, when interpreted together with the findings of structural similarity of flow over rough walls [38–40] suggests that a universal structural similarity is potentially present. The structure observed in Figure 14 does not seem to depend on the FST boundary condition. This is remarkable since the extent of disturbance in this case is over 10% (in FST level), which is stronger than the near-wall peak turbulence intensity in a comparable Reynolds number canonical flow.

It has been well-established in the literature that the outer layer of a canonical boundary layer contains inclined structures that are associated with ejections and sweeps [41, 42]. Adrian *et al.* [43] referred to these structures, which are coherently aligned in the streamwise direction creating a large-scale coherent motion, as the hairpin vortex packets. Their model supported the existence of vortex organisation both in the near-wall and outer layer of the flow. One of the characteristic feature of these packets is the streamwise alignment of a series of hairpin vortices, inclined away from the wall at angles between 12°and 20° [44]. However, the present study is not focused on the specific coherent structures that create this organisation. Here, the structural organisation underlying the correlation contours will be presented. For this purpose, the inclination angle can be estimated from the correlation contours by assuming an

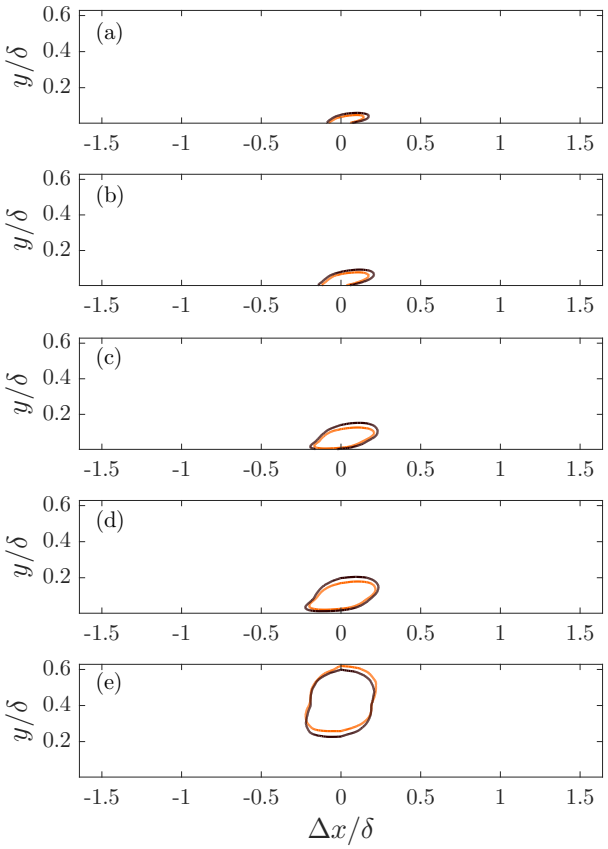

Figure 14. R_{uu} correlation comparison for FST cases at different wall-normal locations (a) y^+≈40 (b) y^+≈100 (c) y^+≈240 (d) y^+≈400 (e) y/δ≈0.4. Representative contour level is 0.25. Orange coloured line: case B, black line: Case D.

elliptical shape for a constant contour level and determining the angle of the major axis of the fitted ellipse. The distribution of this angle across the boundary layer is shown in Figure 15 in comparison with the results from the multi-point measurements using a rake of hot-wire probes performed for the same cases in another study by the authors [6]. The angle from the multi-point hot-wire measurements is computed using the streamwise shift between the inner and outer probe signals by implementing Taylor's hypothesis. The results from these two methods (note that the PIV wall-normal extent is limited compared to the available measurement range of multi-wire measurements) give compatible results for most of the boundary layer. The discrepancy in the outermost region might be due to the use of Taylor's hypothesis for hot-wire data. Nonetheless, the inclination angle of the structures is found to be consistent with the literature and, to reiterate, suggests promising results for the analogy between high Reynolds number flows and the present study cases as the structural organisation inside the boundary layer is not altered despite the external disturbance from FST.

Figure 16 shows R_{uu}, R_{vv} and R_{uv} correlations at two representative wall-normal locations for the two FST cases in comparison. There is essentially no significant difference among the cases for any of the correlations. As mentioned before, an increase in the free-stream turbulence level, i.e. penetration of higher energy fluctuations into the boundary layer, does not affect the extent and size of the structures inside the boundary layer in the plane of interest, i.e. streamwise-wall-normal plane. The sharp drop of R_{vv} correlation at y^+≈100 is worth to note suggesting that the streamwise coherence in v fluctuations is quite short. In the outer region, y/δ≈0.42, the streamwise extent increases due to higher interactions with the free-stream and the direct penetration of FST into the boundary layer in this region, hence the increased v fluctuations. R_{uv} correlations at y^+≈100, similar to R_{uu}, have long streamwise coherence. The negative values also suggest that the low-speed fluid is associated with an upwash over long streamwise distances [36]. There is also slight asymmetry, albeit hardly noticeable, which becomes more apparent in the outer region, y/δ≈0.42.

Representative streamwise and wall-normal length scales can be estimated from the correlations by choosing a contour level [45]. Figure 17 shows these length scales for R_{uu} and R_{vv} correlations in comparison for both cases for

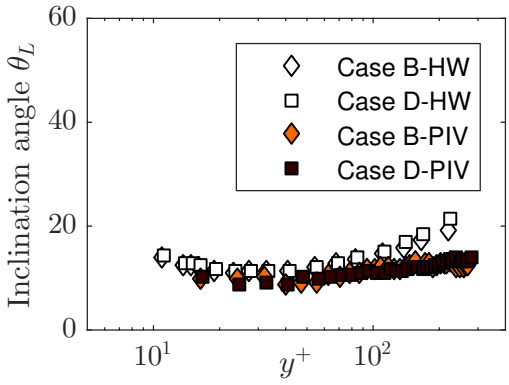

Figure 15. Comparison of the inclination angle, θ_L, obtained through hot-wire and PIV measurements. Symbols are explained in the legend.

a contour level of 0.5. Since the scales are dependent on the chosen contour level, these plots will only reveal the trends of the length scales in the boundary layer. L_x of R_{uu} correlations seem to stay constant for both cases for the wall-normal range presented. This trend is similar to a channel flow [45]. L_y of R_{uu} correlations almost collapse for two cases and show a gradual increase above the log-region. It should be noted that the wall-normal length scales are presented for $y/\delta \geq 0.03$ as, below this location, the contours begin to merge with the wall, and therefore it is difficult to apply a similar analysis of the wall-normal extent.

For L_x of R_{vv}, as shown in Figure 17, it can be seen that the length scales start from quite small values near the wall (almost zero) due to low streamwise coherence of R_{vv} as previously mentioned. For these length scales, the high turbulence case D have slightly higher values than the low turbulence case B above $y/\delta \approx 0.1$ throughout the range shown. This could be justified by different penetration levels of these two cases, as an increased penetration of FST would be associated with higher wall-normal fluctuations in the boundary layer. A decrease of L_y above $y/\delta \approx 0.4$ for case D and above $y/\delta \approx 0.45$ for case B is shown in Figure 17 and this could be related to the uncorrelated free-stream fluctuations dominantly found in this region.

VI. CONCLUSION

This experimental study builds upon the related previous ones [5, 6], which focused on the response of the turbulent boundary layer to high levels of free stream turbulence, to include the insights drawn from statistical and structural information obtained using a PIV measurement technique. It is shown that wall-normal velocity and Reynolds shear stress profiles followed the inner-scaling which has been found contrary to the streamwise fluctuations. Addition of free-stream turbulence into the flow resulted in an extended plateau region around the local peak for Reynolds shear stress profiles. Increasing the level of FST resulted in further extension of that plateau. This effect was found similar to high Reynolds number canonical flows for increasing Re_τ.

Quadrant analysis was employed to determine the contributions of different Reynolds-stress-producing events. The dominant contributors were found to be sweep and ejection events in the boundary layer. The outward and inward interaction events were observed to contribute very little until towards the edge of the boundary layer. These results suggested a degree of similarity in momentum transport between the present cases and channel flows. The common intermittency characteristics of the two flows was believed to play the main role in this similarity.

The structural organisation of the flow was presented using the two-point spatial velocity correlations. This enabled describing the coherence of the turbulent structures in the boundary layer. The streamwise velocity autocorrelations showed structures that are coherent for extended distances in streamwise direction whereas the wall-normal velocity correlations were found to be quite short in streamwise coherence. The inclination angle of these coherent structures was estimated using the correlation contours and the value was found to be consistent with the literature. There appears to be structural similarity across all wall-bounded flows as the structures were found statistically identical with previous studies such as those on smooth and rough walls. This similarity implies that the structural organisation inside the boundary layer was not altered despite the external disturbance from FST. This signifies a potential universal structural representation of wall-bounded flows where the boundary conditions do not change the organisation of the structures but their strength.

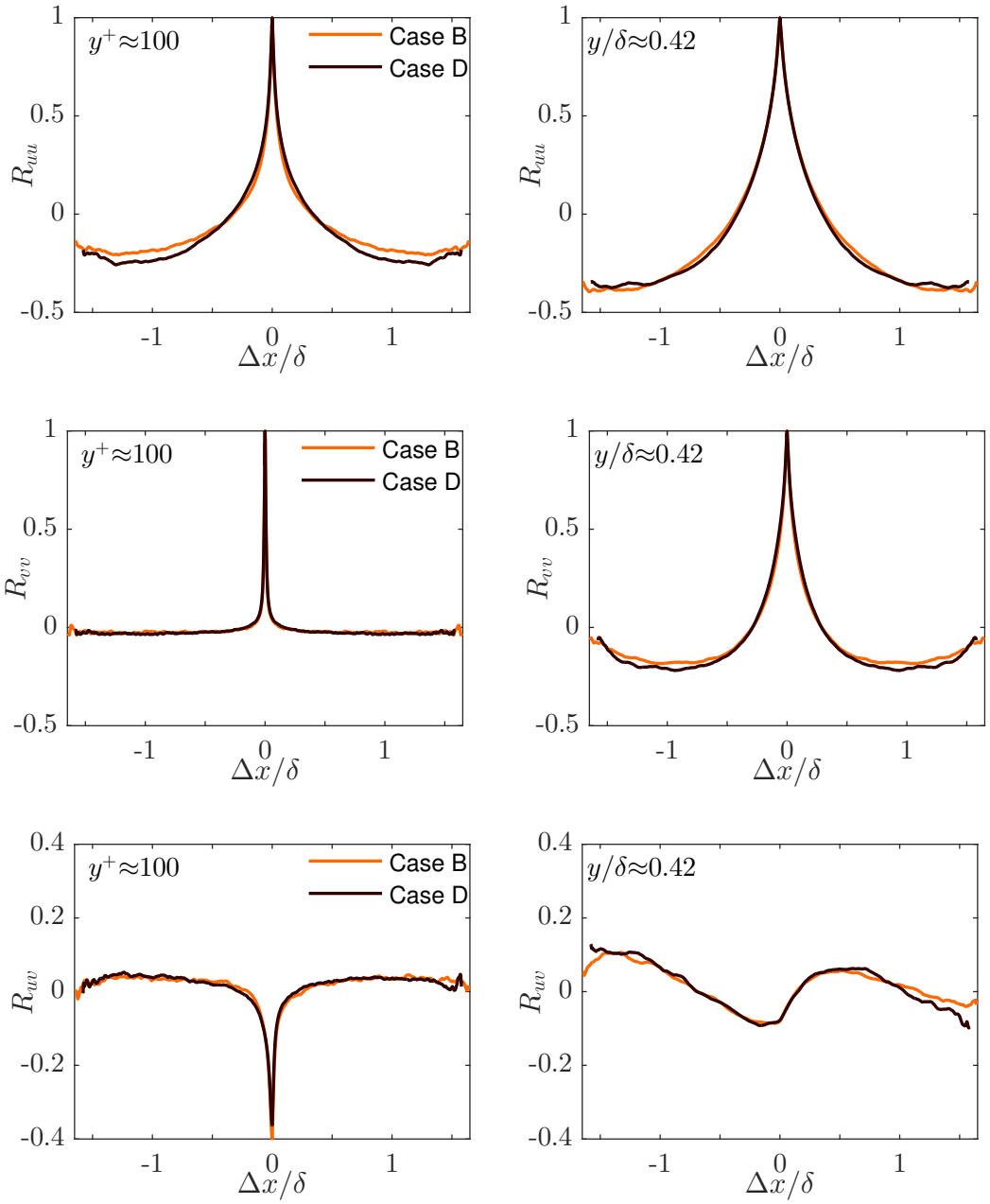

Figure 16. (Top) R_{uu} (middle) R_{vv} (bottom) R_{uv} correlations at (left) $y^+\approx100$ and (right) $y/\delta\approx0.42$ for both FST cases. Orange coloured line: case B, black line: Case D.

ACKNOWLEDGMENTS

The authors acknowledge the financial support of the European Research Council (ERC Grant agreement No. 277472), and the Engineering and Physical Sciences Research Council of the United Kingdom (EPSRC Grant Ref. No. EP/L006383/1). RJH was partially funded by the Natural Sciences and Engineering Research Council of Canada (NSERC) while at the University of Southampton, and is presently supported by the Onsager Fellowship program at

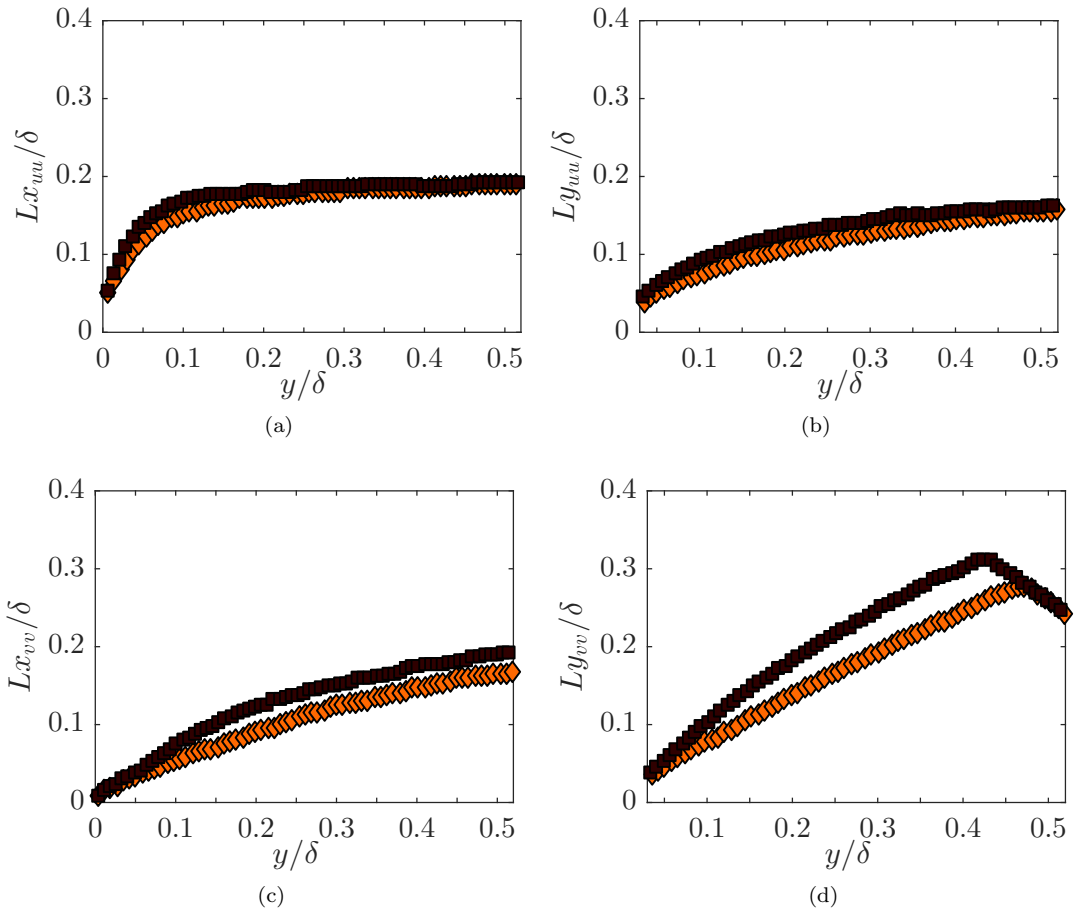

Figure 17. Wall-normal variation of (a, c) streamwise and (b, d) wall-normal length scales based on $R_{uu} = 0.5$ and $R_{vv} = 0.5$ for both FST cases. Case B: filled diamond, case D: filled square.

NTNU. ED was partially funded by Zonta International while at the University of Southampton.

[1] M. F. Blair, "Influence of free-stream turbulence on turbulent boundary layer heat transfer and mean profile development, part i?experimental data," J. Heat Transfer **105**, 33–40 (1983).
[2] P. E. Hancock and P. Bradshaw, "The effect of free-stream turbulence on turbulent boundary layers," J. Fluids Eng. **105(3)**, 284–289 (1983).
[3] J. C. R. Hunt, P. A. Durbin, and X. Wu, *Interactions between freestream turbulence and boundary layers*, Tech. Rep. (Center for Turbulence Research, 1998).
[4] N. S. Sharp, S. Neuscamman, and Z. Warhaft, "Effects of large-scale free stream turbulence on a turbulent boundary layer," Phys. Fluids **21**, 095105 (2009).
[5] E. Dogan, R. E. Hanson, and B. Ganapathisubramani, "Interactions of large-scale free-stream turbulence with turbulent boundary layers," J. Fluid Mech. **802**, 79–107 (2016).
[6] E. Dogan, R. J. Hearst, and B. Ganapathisubramani, "Modelling high Reynolds number wall–turbulence interactions in laboratory experiments using large-scale free-stream turbulence," Phil. Trans. R. Soc. A **375** (2017).
[7] B. Ganapathisubramani, E. K. Longmire, and I. Marusic, "Characteristics of vortex packets in turbulent boundary layers," J. Fluid Mech. **478**, 35–46 (2003).
[8] M. Guala, S. E. Hommema, and R. J. Adrian, "Large-scale and very-large-scale motions in turbulent pipe flow," J. Fluid Mech. **554**, 521–542 (2006).
[9] B. J Balakumar and R. J Adrian, "Large- and very-large-scale motions in channel and boundary-layer flows," Phil. Trans. R. Soc. A **365**, 665–681 (2007).
[10] P. E. Hancock and P. Bradshaw, "Turbulence structure of a boundary layer beneath a turbulent free stream," J. Fluid Mech. **205**, 45–76 (1989).

[11] B. Stefes and H.-H. Fernholz, "Skin friction and turbulence measurements in a boundary layer with zero-pressure-gradient under the influence of high intensity free-stream turbulence," Eur. J. Mech. B **23**, 303–318 (2004).

[12] K. A. Thole and D. G. Bogard, "High freestream turbulence effects on turbulent boundary layers," J. Fluids Eng. **118**, 276–284 (1996).

[13] H. Makita, "Realization of a large-scale turbulence field in a small wind tunnel," Fluid Dyn. Res. **8(2)**, 53–64 (1991).

[14] K.T. Christensen, "The influence of peak-locking errors on turbulence statistics computed from piv ensembles," Exp. Fluids **36**, 484–497 (2004).

[15] R. J. Hearst and B. Ganapathisubramani, "Quantification and adjustment of pixel-locking in particle image velocimetry," Exp. Fluids **56**, 1–5 (2015).

[16] J. V. Larssen and W. J. Devenport, "On the generation of large-scale homogeneous turbulence," Exp. Fluids **50**, 1207–1223 (2011).

[17] R. J. Hearst and P. Lavoie, "The effect of active grid initial conditions on high reynolds number turbulence," Exp. Fluids **56**, 185 (2015).

[18] L. B. Esteban, E. Dogan, E. Rodríguez-López, and B. Ganapathisubramani, "Skin-friction measurements in a turbulent boundary layer under the influence of free-stream turbulence," Exp. Fluids **58**, 115 (2017).

[19] A. E. Perry and J. D. Li, "Experimental support for the attached-eddy hypothesis in zero-pressure-gradient turbulent boundary layers," J. Fluid Mech. **218**, 405–438 (1990).

[20] T. Wei and J. Klewicki, "Scaling properties of the mean wall-normal velocity in zero-pressure-gradient boundary layers," Phys. Rev. Fluids **1**, 082401 (2016).

[21] A. Lozano-Durán and J. Jiménez, "Effect of the computational domain on direct simulations of turbulent channels up to $Re_\tau = 4200$," Phys. Fluids **26**, 011702 (2014).

[22] D. B. De Graaff and J. K. Eaton, "Reynolds-number scaling of the flat-plate turbulent boundary layer," J. Fluid Mech. **422**, 319–346 (2000).

[23] M. H. Buschmann and M. Gad-el Hak, "Normal and cross-flow reynolds stresses: differences between confined and semi-confined flows," Exp. Fluids **49**, 213–223 (2010).

[24] R. Örlü, T. Fiorini, A. Segalini, G. Bellani, A. Talamelli, and P. H. Alfredsson, "Reynolds stress scaling in pipe flow turbulence—first results from ciclope," Phil. Trans. R. Soc. A **375** (2017).

[25] H. S. Kang, S. Chester, and C. Meneveau, "Decaying turbulence in an active-grid-generated flow and comparisons with large-eddy simulation," J. Fluid Mech. **480**, 129–160 (2003).

[26] P. J. A. Priyadarshana and J. C. Klewicki, "Study of the motions contributing to the reynolds stress in high and low reynolds number turbulent boundary layers," Phys. Fluids **16**, 4586–4600 (2004).

[27] E. R. Corino and Robert S. Brodkey, "A visual investigation of the wall region in turbulent flow," J. Fluid Mech. **37**, 1–30 (1969).

[28] J. M. Wallace, H. Eckelmann, and R. S. Brodkey, "The wall region in turbulent shear flow," J. Fluid Mech. **54**, 39–48 (1972).

[29] S. S. Lu and W. W. Willmarth, "Measurements of the structure of the reynolds stress in a turbulent boundary layer," J. Fluid Mech. **60**, 481–511 (1973).

[30] R. J. Adrian, "Hairpin vortex organization in wall turbulence," Phys. Fluids **19**, 041301 (2007).

[31] J. Jiménez, S. Hoyas, M. P. Simens, and Y. Mizuno, "Turbulent boundary layers and channels at moderate reynolds numbers," J. Fluid Mech. **657**, 335–360 (2010).

[32] W. W. Willmarth and S. S. Lu, "Structure of the Reynolds stress near the wall," J. Fluid Mech. **55**, 65–92 (1972).

[33] D. G. Bogard and W. G. Tiederman, "Burst detection with single-point velocity measurements," J. Fluid Mech. **162**, 389–413 (1986).

[34] A. Lozano-Durán, O. Flores, and J. Jiménez, "The three-dimensional structure of momentum transfer in turbulent channels," J. Fluid Mech. **694**, 100–130 (2012).

[35] J. M. Wallace, "Space-time correlations in turbulent flow: A review," Theor. Appl. Mech. Lett. **4**, 022003– (2014).

[36] B. Ganapathisubramani, N. Hutchins, W. T. Hambleton, E. K. Longmire, and I. Marusic, "Investigation of large-scale coherence in a turbulent boundary layer using two-point correlations," J. Fluid Mech. **524**, 57–80 (2005).

[37] M. Tutkun, W. K. George, J. Delville, M. Stanislas, P. B.V. Johansson, J.-M. Foucaut, and S. Coudert, "Two-point correlations in high Reynolds number flat plate turbulent boundary layers," J. Turbul. **10**, 1–23 (2009).

[38] J. Jiménez, "Turbulent flows over rough walls," Annu. Rev. Fluid Mech. **36**, 173–196 (2004).

[39] K. A. Flack, M. P. Schultz, and T. A. Shapiro, "Experimental support for Townsend's Reynolds number similarity hypothesis on rough walls," Phys. Fluids **17**, 035102– (2005).

[40] M. Placidi, *On the effect of surface morphology on wall turbulence*, Ph.D. thesis, University of Southampton (2015).

[41] G. L. Brown and A. S. W. Thomas, "Large structure in a turbulent boundary layer," Phys. Fluids **20**, S243–S252 (1977).

[42] M. R. Head and P. Bandyopadhyay, "New aspects of turbulent boundary-layer structure," J. Fluid Mech. **107**, 297–338 (1981).

[43] R. J. Adrian, C. D. Meinhart, and C. D. Tomkins, "Vortex organization in the outer region of the turbulent boundary layer," J. Fluid Mech. **422**, 1–54 (2000).

[44] K. T. Christensen and J. R. Adrian, "Statistical evidence of hairpin vortex packets in wall turbulence," J. Fluid Mech. **431**, 433–443 (2001).

[45] K. T. Christensen and Y. Wu, "Characteristics of vortex organization in the outer layer of wall turbulence," in *TSFP Digitial Library Online* (Begel House Inc., 2005).